Phthalocyanine Precursors To Construct Atomically Dispersed Iron Electrocatalysts

Yang Wang,[†,‡] Maoyu Wang,[§] Zisheng Zhang,[†] Qi Wang,[†] Zhan Jiang,[†,‡] Marcos Lucero,[§] Xing Zhang,[†] Xiaoxiao Li,[†] Meng Gu,*[,†] Zhenxing Feng,*[,§] and Yongye Liang*[,†]

[†]Department of Materials Science and Engineering, Southern University of Science and Technology, Shenzhen 518055, China

[‡]School of Materials Science and Engineering, Harbin Institute of Technology, Harbin 150001, China

[§]School of Chemical, Biological and Environmental Engineering, Oregon State University, Oregon 97331, United States

S *Supporting Information*

ABSTRACT: Carbon materials embedded with atomically dispersed metal sites have recently demonstrated intriguing performance as electrocatalysts. However, it remains challenging to construct abundant single metal atoms due to easy aggregation of metal species during the high-temperature synthesis. Herein, a facile method is devloped to construct single iron atom electrocatalysts with high iron content by employing iron phthalocyanine (FePc) derivatives as metal precursors. FePc molecules are encapsulated into the zeolitic imidazolate frameworks (ZIFs), and the subsequent pyrolysis yields the catalysts. Cyano substitution on FePc ($FePc(CN)_8$) can facilitate introduction of phthalocyanine molecules and formation of active sites, thus affording higher activity for the oxygen reduction reaction than the FePc counterpart. It is also found that adding iron salt with $FePc(CN)_8$ can afford a better catalyst with enhanced surface $Fe-N_x$ content, which exhibits high activities with a half-wave potential of 0.910 and 0.811 V versus reversible hydrogen electrode in alkaline and acidic conditions, respectively. Moreover, $FePc(CN)_8$/ZIF-derived catalyst exhibits high selectivities and good activities for carbon monoxide production in the carbon dioxide reduction reaction (CO_2RR). The bulk $Fe-N_x$ sites are found to be more stable than the surface $Fe-N_x$ sites possibly due to the improved desorption of carbon monoxide.

KEYWORDS: oxygen reduction reaction, carbon dioxide reduction reaction, iron phthalocyanine, single-atom electrocatalysts, zeolitic imidazolate frameworks
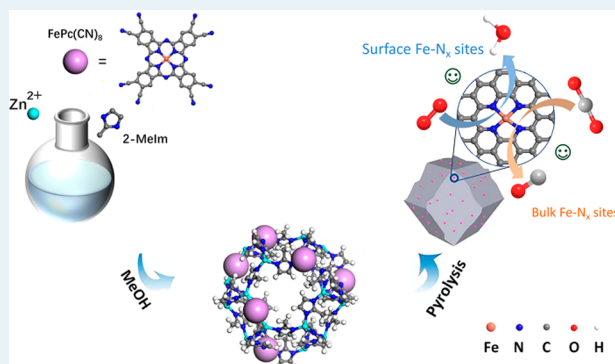
INTRODUCTION

The oxygen reduction reaction (ORR) is an important cathodic reaction for energy conversion technologies, such as fuel cells. ORR catalysis presents a bottleneck for the efficiency and commercial viability of these promising energy technologies due to its sluggish reaction kinetics. Pt-based catalysts exhibit the highest performance, especially in acidic conditions, but suffers from high cost and scarcity.[1−3] Significant advances have been demonstrated to improve the mass activities of Pt by a variety of methods, including alloying and nanostructuring.[4−6] Alternatively, extensive efforts have been devoted to develop nonprecious metal-based catalysts.[7−10] Among them, the carboneous materials embedded with nitrogen-coordinated transition metals (Me−N−C) are promising candidates, exhibiting high activities even comparable to Pt-based catalysts in alkaline conditions, though their performance in acidic condition is still inferior.[11,12]

Active Fe−N−C-based catalysts are often constructed with high surface area substrates. Dodelet et al. synthesized an Fe−N−C catalyst by mixing iron(II) acetate ($FeAc_2$) and 1,10-

phenanthroline (Phen) with Black Pearl carbon.[13] The cathode current density with this Fe−N−C catalyst (5.3 mg cm^{-2}) can be comparable with Pt-based catalyst (0.4 mg cm^{-2}). Later, a high surface area zeolitic imidazolate framework (ZIF), ZIF-8, was employed as the substrate for $FeAc_2$ and Phen, and the resulted catalyst demonstrated enhanced current density and power density compared to those of Black Pearls counterpart.[14] However, such physical mixing of iron precursors with carbon substrates could easily cause aggregation of iron species during the high-temperature treatment, forming large iron particles, which could negatively affect the catalytic performance.[15−19] Li et al. reported that the cage confinement of $Fe(AcAc)_3$ in ZIF-8 could prevent the aggregation of iron species and produce the single iron atom-dispersed catalyst during pyrolysis.[20] Very recently, Wu et al. reported an elegant method to synthesize Fe−N−C catalysts with atomically

Scheme 1. Synthetic Method for Catalysts with Fe–N$_x$ Sites Embedded in Carbon from Iron Phthalocyanine Molecules
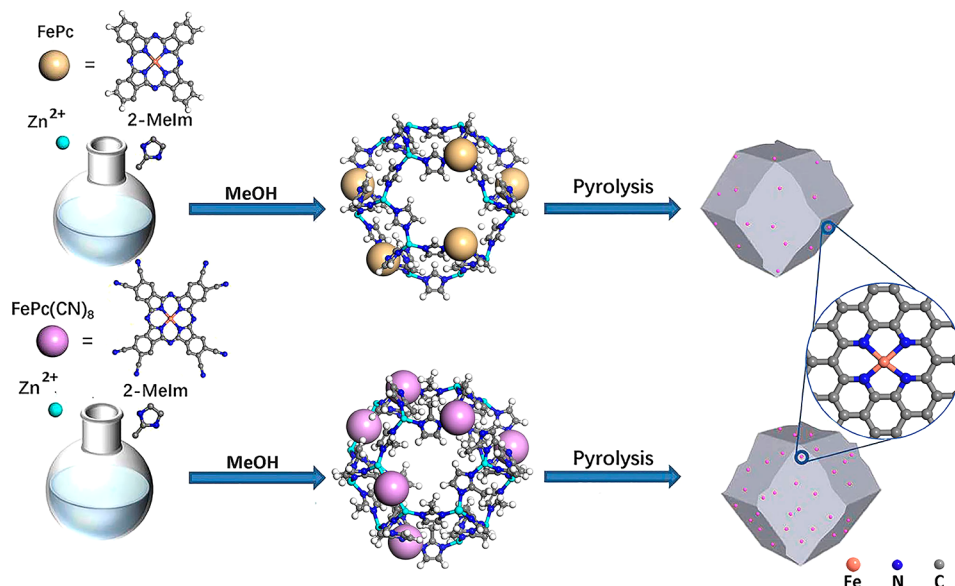
dispersed iron by pyrolyzing iron-doped ZIF-8 with controlled particle size. Iron is fixed by the coordination with the imidazole ligand to prevent aggregation, and the iron content can be as high as 0.45 atom % in the carbonized product. The optimized catalyst can catalyze ORR with a half-wave potential ($E_{1/2}$) of 0.85 V (all of the potentials are versus reversible hydrogen electrode (RHE) otherwise noted) in acidic media.[21]

Since the discovery of catalytic activities for ORR in 1964, metal phthalocyanines and porphyrins with the metal–N$_4$-coordinated structure have attracted much attention as ORR catalysts due to their good stability and structural tunability.[22−24] However, the activities of primitive molecules are partially limited by their poor electronic conductivity.[25,26] High-temperature treatments can afford better ORR activities, especially in acidic conditions. However, such treatment generally results in aggregation of metal species to form less active metal particles.[27,28] Joo et al. dispersed the iron porphyrin molecules on carbon nanotubes and introduced a silica coating to reduce the substantial Fe aggregation during pyrolysis.[29] The ORR activity of the produced sample with silica coating is higher ($E_{1/2}$ = 0.88 V) than that without silica coating (0.85 V) in alkaline conditions. However, such synthetic process is still not efficient to prevent the aggregation of Fe species.

Herein, we present a facile approach to synthesize Fe–N–C catalysts with atomically dispersed iron sites from ZIF-8 by employing FePc-based molecules as metal precursors. FePc molecules are first encapsulated in the frameworks of ZIFs during their synthesis, and subsequent pyrolysis yields the Fe–N–C materials. Octacyano substitution on FePc (FePc(CN)$_8$) can facilitate the incorporation of phthalocyanine molecules into ZIF to afford higher iron loading and more active sites in the carboneous network compared to original FePc. Transmission electron microscopy (TEM) and X-ray absorption spectroscopy (XAS) studies reveal the prevalent presence of single iron atoms in these materials even at a high iron loading of 2.60 wt %. The catalyst derived from FePc(CN)$_8$/ZIF-8 exhibits higher activities for ORR than other catalysts derived from FePc/ZIF-8, Fe(AcAc)$_3$/ZIF-8, as well as the FePc(CN)$_8$ physically absorbed in ZIF-8. Further, it is found that the ORR

catalytic activities in acidic condition are correlated with the content of surface Fe–N$_x$ sites. Adding iron salt during the preparation of FePc(CN)$_8$/ZIF-8 can afford a better catalyst with enhanced surface Fe–N$_x$ content. Such catalyst exhibits an $E_{1/2}$ of 0.811 and 0.910 V in acid and alkaline conditions, respectively. Moreover, these atomically dispersed iron atom catalysts also exhibit good catalytic performance for carbon dioxide reduction (CO$_2$RR). The FePc(CN)$_8$-derived catalyst could deliver a reduction current density of −5 mA/cm² and a Faradaic efficiency (FE) for CO production of around 94% at −0.46 V. It is also found that the bulk Fe–N$_x$ sites exhibit better stability than the surface sites in CO$_2$RR.

■ RESULTS AND DISCUSSION

Scheme 1 illustrates the synthetic procedure of the Fe–N–C catalysts (details are given in the Experimental Section). The FePc molecules can be incorporated into ZIF-8 by the coordination between the iron center and 2-methylimidazole (Figure S1). Subsequent carbonization at 1000 °C was performed to convert FePc/ZIF-8 to the carboneous product (denoted as C-FePc/ZIF-8). The iron content can be tuned by varying the added FePc amount during the synthesis, and the highest iron content can reach 2.20 wt % (determined by inductively coupled plasma mass spectrometry (ICP-MS)) without detection of aggregative iron species. It is further found that the cyano group in FePc(CN)$_8$ can facilitate the incorporation of phthalocyanine molecules into ZIF-8 possibly due to the coordination between the cyano group and the Zn ion (Figure S1). The C-FePc(CN)$_8$/ZIF-8 product can reach a higher Fe content limit of 2.60 wt %.

The crystalline structures of the ZIF precursors and the produced catalysts were measured by X-ray diffraction (XRD) (Figure S2a). The carbonized products exhibit two main diffraction peaks at around 24.8° and 44.1° (Figure S2b), corresponding to the (002) and (101) crystalline planes of carbon, respectively. No metallic Fe crystal phases are observed. TEM images show that the FePc- and FePc(CN)$_8$-incorporated ZIF-8 precursors retain the dodecahedral structure of pure ZIF-8 with slight distortion, and the particle size is around 180 nm (Figure S3). After high-temperature
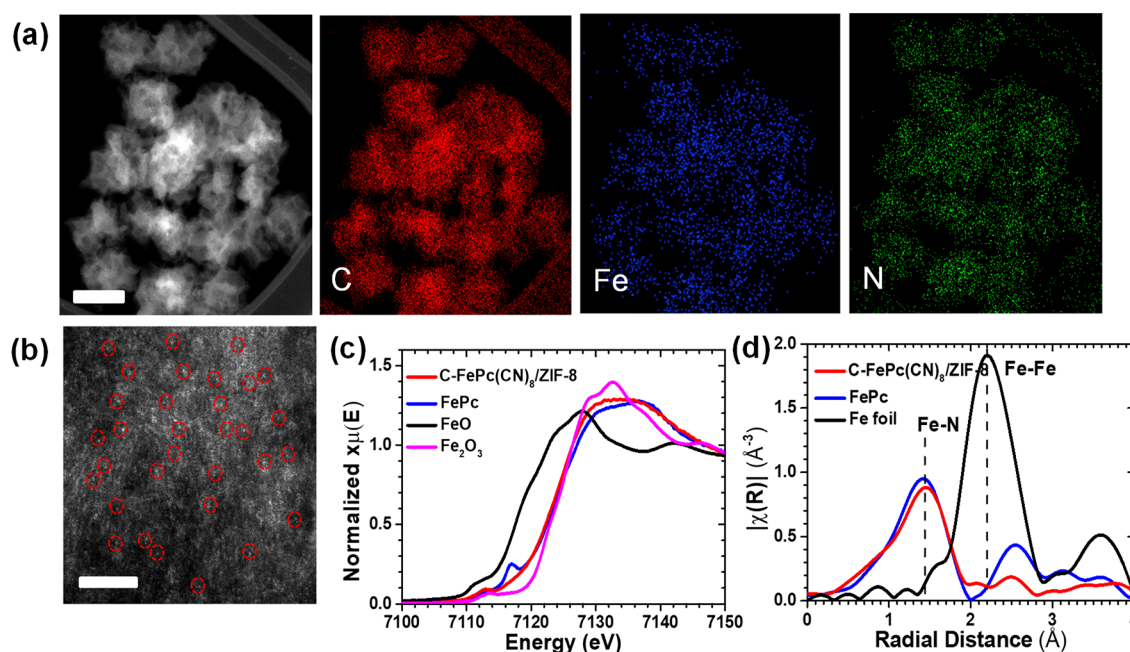
Figure 1. Morphological and structural characterization of C-FePc(CN)$_8$/ZIF-8. (a) STEM image of the C-FePc(CN)$_8$/ZIF-8 sample, and corresponding elemental maps showing the homogeneous distribution of C (red), Fe (blue), and N (green) (scale bar is 100 nm). (b) HAADF-STEM image of C-FePc(CN)$_8$/ZIF-8. Bright metal atoms are highlighted by red circles (scale bar is 5 nm). (c) Fe K-edge XANES for C-FePc(CN)$_8$/ZIF-8, FePc, FeO, and Fe$_2$O$_3$. (d) Fe K-edge EXAFS spectra of FePc(CN)$_8$/ZIF-8, FePc, and Fe foil.
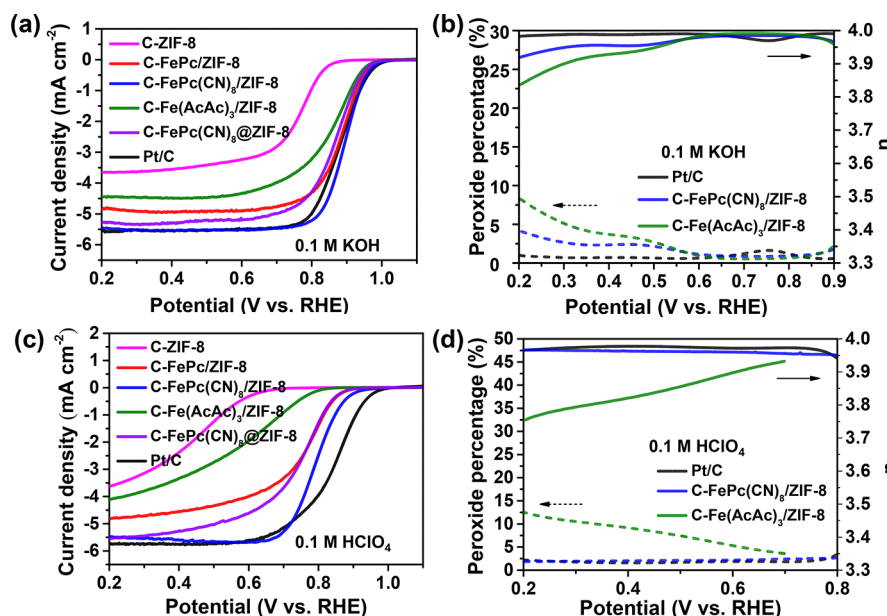

Figure 2. Electrocatalytic performance for ORR. (a) ORR polarization plots for the prepared catalysts and Pt/C in O$_2$-saturated 0.1 M KOH at 1600 rpm. Current in N$_2$-saturated 0.1 M KOH was deducted. Catalyst loading is 0.2 mg cm^{-2} for the prepared catalysts and 0.1 mg cm^{-2} for Pt/C. (b) Peroxide yield (dashed) and *n* (solid) for the catalysts determined by RRDE in 0.1 M KOH. (c) ORR polarization plots for the prepared catalysts and Pt/C catalysts in O$_2$-saturated 0.1 M HClO$_4$ at 1600 rpm. Current in N$_2$-saturated 0.1 M HClO$_4$ was dedected. Catalyst loading is 0.6 mg cm^{-2} for the prepared catalysts and 0.1 mg cm^{-2} for Pt/C. (d) Peroxide yield (dashed) and *n* (solid) for the catalysts determined by RRDE in 0.1 M HClO$_4$.

treatment, the carbonized products maintain a similar particle size but the dodecahedral structure collapses (Figure 1a). BET (Brunauer−Emmett−Teller) measurement confirms the porous structure of the carbonized products with the predomination of micropores (Figure S4 and Table S1). The energy-dispersive spectroscopy (EDS) elemental mappings suggest a homogeneous distribution of C, Fe, and N elements in C-

FePc(CN)$_8$/ZIF-8 (Figure 1a). Atomically dispersed metal sites are clearly identified (highlighted by red cycles) by the atomic-resolution high-angle annular dark-field scanning transmission electron microscope (HAADF-STEM) measurement (Figure 1b), and no aggregated metallic species are observed even for the sample with a high iron loading of 2.60 wt % (see detailed ICP-MS results in Table S2). Electron energy loss
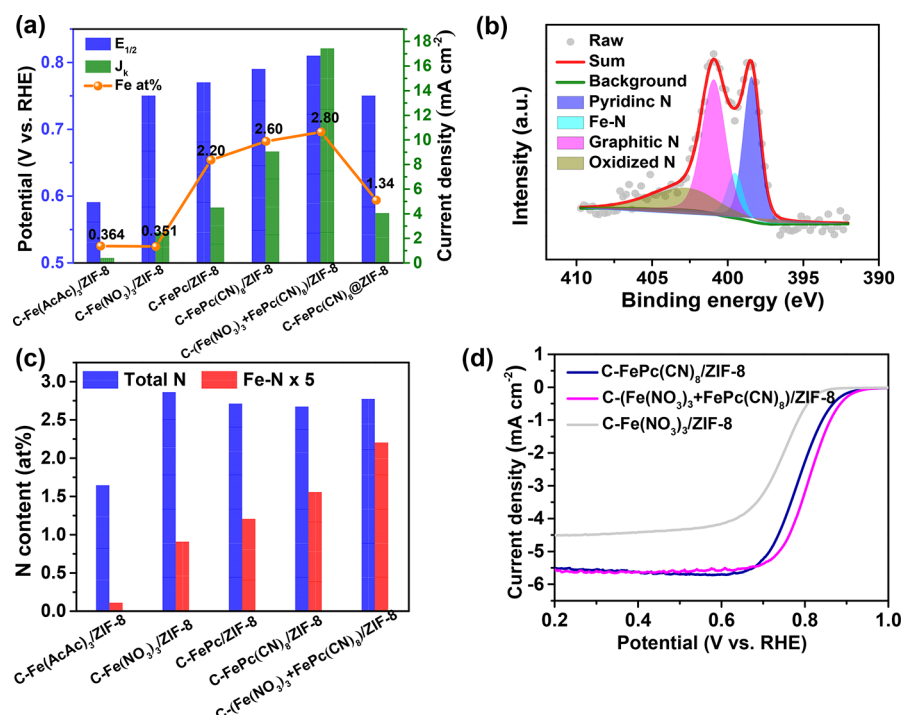
Figure 3. Dependence of ORR catalytic activity and surface $Fe-N_x$ content. (a) Correlation between $E_{1/2}$ (blue), J_k (at 0.75 V) (green) in 0.1 M $HClO_4$ and Fe content (wt %, determined by ICP-MS) for the prepared catalysts. (b) N 1s spectrum of $C-FePc(CN)_8/ZIF-8$. (c) Total N content and 5-fold of surface $Fe-N_x$ content of the prepared catalysts determined by XPS. (d) ORR polarization plots for $C-FePc(CN)_8/ZIF-8$, $C-(Fe(NO_3)_3+FePc(CN)_8)/ZIF-8$, and $C-Fe(NO_3)_3/ZIF-8$ in O_2-saturated 0.1 M $HClO_4$ at 1600 rpm. Current in N_2-saturated 0.1 M $HClO_4$ was deducted. Catalyst loading is 0.6 mg cm^{-2}.

spectroscopy (EELS) on the bright metallic spots shows the Fe^{2+} 2L peaks, suggesting the coordinated structure of Fe and N in the catalyst (Figure S5). In contrast, significant Fe aggregation is observed in $C-Fe(AcAc)_3/ZIF-8$ prepared by the same method but replacing FePc with $Fe(AcAc)_3$ (Figures S6 and S7).

The X-ray absorption near-edge structure (XANES) of Fe K-edge in Figure 1c shows that the edge of $C-FePc(CN)_8/ZIF-8$ is located between Fe_2O_3 and FeO, similar to the catalyst prepared from Fe-doped ZIF-8.[21,30] It is noted that the XANES of $C-FePc(CN)_8/ZIF-8$ also overlaps with that of FePc, indicating the possible remaining $Fe-N_4$ structure. The Fourier-transformed extened X-ray adsorption fine structure (EXAFS) curves show that the dominate peak in $C-FePc(CN)_8/ZIF-8$ can be assigned to $Fe-N_x$ coordination and no Fe–Fe coordination exists in Figure 1d (and Figure S8), confirming the absence of Fe metallic clusters in the catalyst.[31] In addition, the first shell (1 Å < R < 2 Å) in EXAFS of $C-FePc(CN)_8/ZIF-8$ overlaps with that of FePc, which may suggest the prescence of a similar coordination structure unit, which is consistent with XANES in Figure 1c. Thermal gravimetric analysis (TGA) reveals the better thermal stability of $FePc(CN)_8$ than that of $Fe(AcAc)_3$ (Figure S9). Thus, $Fe(AcAc)_3$ is easier to decompose and form aggregation under high-temperature treatment. In contrast, the higher thermal stability of FePc or $FePc(CN)_8$ molecules and the coordination between the iron center and the imidazole could prevent the aggregation of Fe species.

To evaluate the catalytic activities of ORR, the as-obtained catalysts and the benchmark Pt/C (20 wt %) were first tested by linear sweep voltammetry (LSV) measurements in 0.1 M O_2-saturated KOH solution. The catalysts derived from FePc-

based molecules exhibit substantially higher catalytic activities than the counterparts derived from original ZIF-8 or $Fe(AcAc)_3$. $C-FePc(CN)_8/ZIF-8$ exhibits an $E_{1/2}$ of 0.901 V, outperforming $C-FePc/ZIF-8$ (0.881 V) and $C-Fe(AcAc)_3/ZIF-8$ (0.862 V) (Figure 2a). Rotating ring disk electrode (RRDE) measurement was employed to study the pathway of the ORR process. As shown in Figure 2b, the electron transfer number (n) of $C-FePc(CN)_8/ZIF-8$ is above 3.93 from 0.2 to 0.9 V, suggesting close to 4e selectivity for oxygen reduction to hydroxide. The $E_{1/2}$ of $C-FePc(CN)_8/ZIF-8$ shifts slightly after 10 000 CV cycles, which indicates the good catalytic stability in alkaline solutions (Figure S10). In contrast, the $E_{1/2}$ of $C-Fe(AcAc)_3/ZIF-8$ negatively shifts 32 mV (Figure S11). These results suggest that the FePc-derived catalysts show good performance for ORR in alkaline condition.

The catalytic performance of these catalysts in acid condition was further studied in 0.1 M O_2-saturated $HClO_4$. The ORR in acid condition is favored due to the potential of proton exchange membrane fuel cells, but it is more challenging because of the sluggish kinetics and corrosiveness.[21] The activities of the prepared catalysts in acid condition decrease as the $E_{1/2}$s are negatively shifted compared to those in basic condition. The activity trend still maintains for the prepared catalysts, and $C-FePc(CN)_8/ZIF-8$ is the best with an $E_{1/2}$ of 0.792 V. However, the $E_{1/2}$ of $C-Fe(AcAc)_3/ZIF-8$ is 0.585 V and negatively shifts 51 mV after 10 000 CV cycles in acidic contions (Figure S11b).

The measured peroxide yields of $C-FePc(CN)_8/ZIF-8$ and $C-FePc/ZIF-8$ remain low (0.2–0.8 V), and the calculated n is above 3.93 (Figure 2d and Figure S12). Notably, the activity difference becomes more obvious in acidic conditions. For example, the $E_{1/2}$ of $C-Fe(AcAc)_3/ZIF-8$ is 205 mV more
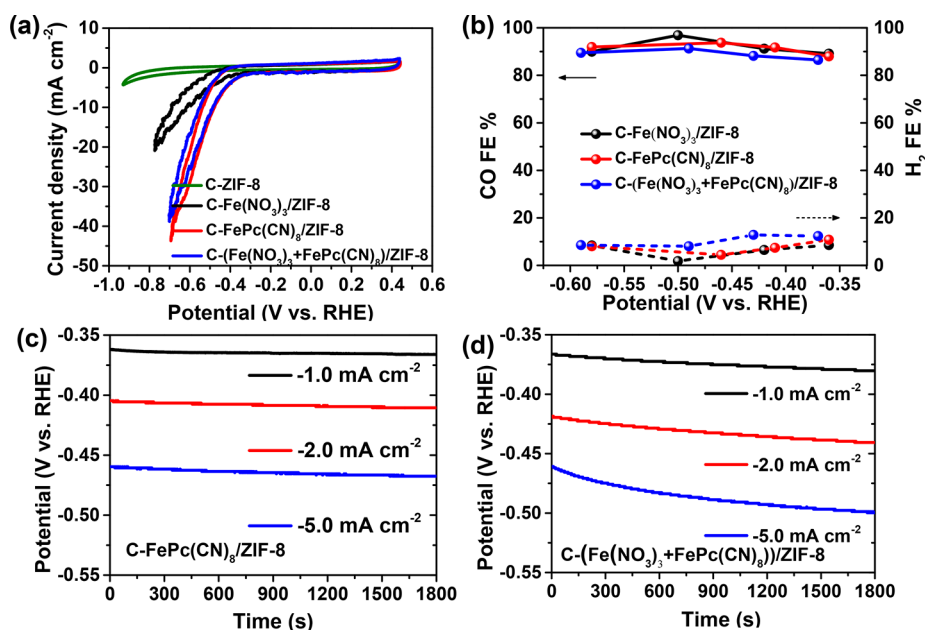
Figure 4. Electrocatalytic CO_2RR performance of the prepared catalysts. (a) Cyclic voltammograms at 20 mV s^{-1}. (b) Faradaic efficiency of CO and H_2. (c) Chronopotentiometry at -1.0, -2.0, and -5.0 mA cm^{-2} of C-FePc(CN)$_8$/ZIF-8. (d) Chronopotentiometry at -1.0, -2.0, and -5.0 mA cm^{-2} of C-(Fe(NO$_3$)$_3$+FePc(CN)$_8$)/ZIF-8. All data are *iR* corrected.

negative than C-FePc(CN)$_8$/ZIF-8, while it is only 39 mV in alkaline condition. Interestingly, the catalyst derived from physical adsorption of FePc(CN)$_8$ in ZIF-8 (denoted as C-FePc(CN)$_8$@ZIF-8) shows higher activities than C-Fe(AcAc)$_3$/ZIF-8, but it is significantly inferior to C-FePc(CN)$_8$/ZIF-8 (Figure 2c). TEM images reveal that aggregated iron particles are found and more significant distortion of the ZIF structure in C-FePc(CN)$_8$@ZIF-8 (Figure S13), which can account for the inferior performance. It suggests that incorporation of FePc(CN)$_8$ molecules in the framework of ZIF-8 can reduce the aggregation of iron species and benefit the active site production in C-FePc(CN)$_8$/ZIF-8.

As Fe−N$_x$ is considered as the catalytic active site for ORR (especially in acid),[32,33] iron content should be correlated with the ORR activities in single iron atom catalysts. Figure 3a shows the plots of $E_{1/2}$ and kinetic current density (J_k) at 0.75 V in the acidic condition versus iron content (from ICP-MS) of the as-obtained catalysts. The $E_{1/2}$ and J_k increase with the iron content. The iron content in C-Fe(AcAc)$_3$/ZIF-8 (0.364 wt %) and C-Fe(NO$_3$)$_3$/ZIF-8 (0.351 wt %) is much lower than that of C-FePc/ZIF-8, which can explain the lower activities in C-Fe(AcAc)$_3$/ZIF-8 and C-Fe(NO$_3$)$_3$/ZIF-8. It also reveals that FePc molecules are easier to be incorporated into the ZIF framework. It is noted that C-Fe(NO$_3$)$_3$/ZIF-8 shows much higher catalytic activities than C-Fe(AcAc)$_3$/ZIF-8, though their iron content is similar (Figure 3a). We also compare a series of C-FePc(CN)$_8$/ZIF-8 catalysts with iron content from 0.12 to 3.16 wt % (Figure S14). The $E_{1/2}$ increases with iron content until 2.60 wt %. Interestingly, the $E_{1/2}$ of C-FePc(CN)$_8$/ZIF-8 with an iron content of 1.66 wt % is similar to that of C-FePc/ZIF-8 with an iron content of 2.20 wt %. The result may suggest that the cyano group can also facilitate introduction of Fe−N$_x$ sites in carbonaceous networks due to functionalization of the phthalocyanine ring.[34−36]

We further used XPS to investigate the surface composition of the prepared catalysts (Figures S15−S17). Due to the low Fe content, the iron spectrum cannot be clearly distinguished.

However, the content of the active Fe−N$_x$ species can be derived from the nitrogen spectrum in Figure 3b (Figure S16). C-FePc(CN)$_8$/ZIF-8 exhibits a similar nitrogen content with C-Fe(NO$_3$)$_3$/ZIF-8 and C-FePc/ZIF-8 in Figure 3c (Table S3). The N 1s peak in Figure 3b (Figure S16) can be separated into 4 types of N: pyridinic N (398.5 eV), Fe−N$_x$ (399.6 eV), graphitic N (400.9 eV), and oxidized N (402.9 eV).[21,29,37−39] It is noted that the Fe−N$_x$ content has a good correlation with the ORR activities. The determined Fe−N$_x$ content is 0.310 atom % for C-FePc(CN)$_8$/ZIF-8, which is higher than that of C-FePc/ZIF-8 (0.241 atom %) and C-Fe(NO$_3$)$_3$/ZIF-8 (0.181 atom %). Although C-Fe(NO$_3$)$_3$/ZIF-8 has a similar bulk iron content (determined from ICP-MS) with C-Fe(AcAc)$_3$/ZIF-8, the surface Fe−N$_x$ content measured from the XPS analysis is much higher than that of C-Fe(AcAc)$_3$/ZIF-8 (0.02 atom %), which explains the higher activity of C-Fe(NO$_3$)$_3$/ZIF-8. These results reveal that the ORR activities are highly related to the surface Fe−N$_x$ content (or Fe content) instead of the bulk iron content. The relatively high ratio of surface Fe−N$_x$ content to bulk Fe content in C-Fe(NO$_3$)$_3$/ZIF-8 suggests that Fe(NO$_3$)$_3$ could facilitate the enrichment of iron species on the surface compared to FePc-based molecules. The STEM observations also suggest this result (Figure S18). By adjusting the defocus (from 0 to 6 nm below the surface), the number of bright iron atoms decreases in the C-Fe(NO$_3$)$_3$/ZIF-8 sample, while it remains similar in the C-FePc(CN)$_8$/ZIF-8 sample.

Inspired by this finding, we further prepared a sample (C-(Fe(NO$_3$)$_3$+FePc(CN)$_8$)/ZIF-8) by mixing Fe(NO$_3$)$_3$ and FePc(CN)$_8$ during the ZIF-8 synthesis to enhance the surface Fe−N$_x$ sites. Single metal atoms are clearly identified, and no aggregated metallic species are observed for C-Fe(NO$_3$)$_3$/ZIF-8 and C-(Fe(NO$_3$)$_3$+FePc(CN)$_8$)/ZIF-8 (Figures S19 and S20). C-(Fe(NO$_3$)$_3$+FePc(CN)$_8$)/ZIF-8 exhibits slightly higher Fe content (2.80 wt %) than C-FePc(CN)$_8$/ZIF-8. However, the surface Fe−N$_x$ content shows a substantial increase to 0.441 atom % compared to 0.310 atom % in C-FePc(CN)$_8$/ZIF-8. In 0.1 M HClO$_4$, C-(Fe(NO$_3$)$_3$+FePc-

$(CN)_8$)/ZIF-8 can deliver an $E_{1/2}$ at 0.811 V, which is 19 mV more positive than that of C-FePc$(CN)_8$/ZIF-8 due to more surface Fe−N$_x$ sites (Figure 3d). This performance is comparable with the best nonprecious metal-based catalysts reported so far (Tables S4 and S5).[29,38,40−43] It also exhibits favorable 4e reduction in the surveyed potential range (Figure S21) and good catalytic stability with only 23 mV decay after 10 000 CV cycles, which is better than C-Fe$(NO_3)_3$/ZIF-8 (Figures S11 and S22). In addition to the enhanced ORR performance in acidic solution, C-(Fe$(NO_3)_3$+FePc$(CN)_8$)/ZIF-8 also shows high activities ($E_{1/2}$ = 0.910 V), good selectivity, and stability in alkaline condition, superior to C-Fe$(NO_3)_3$/ZIF-8 (Figures S11 and S23). The Tafel slopes for C-(Fe$(NO_3)_3$+FePc$(CN)_8$)/ZIF-8 at low overpotential in both alkaline (57 mV dec^{-1}) and acid (59 mV dec^{-1}) conditions are close to 60 mV dec^{-1} (Figure S24). It suggests that the rate-determining step for the C-(Fe$(NO_3)_3$+FePc$(CN)_8$)/ZIF-8 catalyst is the first electron reduction of oxygen for ORR.[44−46]

Fe−N$_x$ sites are also reported as active sites to reduce CO_2 to CO.[33,47−50] The electrochemical performance of our catalysts for CO_2RR was studied in a CO_2-saturated 0.5 M $KHCO_3$ aqueous solution. The iron-containing catalysts exhibit significant reduction current at potentials below ca. −0.31 V (Figure 4a). Due to the higher iron content of C-FePc$(CN)_8$/ZIF-8, its reduction current densities are significantly larger than those of C-Fe$(NO_3)_3$/ZIF-8 at the same potentials. Surprisingly, C-(Fe$(NO_3)_3$+FePc$(CN)_8$)/ZIF-8 does not exhibit a larger reduction current than C-FePc$(CN)_8$/ZIF-8 despite its higher iron content. Electrochemical CO_2 reduction was further performed under controlled current densities, and the gas products were analyzed by gas chromatography (GC) to determine FE (Figure 4b−d). The FEs of CO for C-FePc$(CN)_8$/ZIF-8, C-(Fe$(NO_3)_3$+FePc$(CN)_8$)/ZIF-8, and C-Fe$(NO_3)_3$/ZIF-8 are all over 89.0% at the surveyed potentials from −0.36 to −0.60 V (Figure 4b).

It should be noted that C-ZIF-8 exhibits a small reduction current at these potentials, and little CO gas was detected (Figure S25), confirming that Fe−N$_x$ sites are the active sites for CO_2RR. C-FePc$(CN)_8$/ZIF-8 exhibits a reduction current density of −5.0 mA/cm^2 and a turnover frequency (TOF) of 0.13 s^{-1} (assuming all Fe atoms are catalytically active) at −0.46 V with a FE for CO of 94%, which is among the best performance for Fe based catalysts for CO_2RR reported so far (Table S6, Supporting Information). C-(Fe$(NO_3)_3$+FePc$(CN)_8$)/ZIF-8 exhibits worse stability than C-FePc$(CN)_8$/ZIF-8 (Figure 4c and 4d). For example, the overpotential of the C-(Fe$(NO_3)_3$+FePc$(CN)_8$)/ZIF-8 electrode increases about 40 mV after chronopotentiometry test at −5.0 mA cm^{-2} for 30 min, while C-FePc$(CN)_8$/ZIF-8 exhibits little increase. Such worse stability of C-(Fe$(NO_3)_3$+FePc$(CN)_8$)/ZIF-8 may explain its lower activities when comparing with C-FePc$(CN)_8$/ZIF-8. It should be pointed out that C-(Fe$(NO_3)_3$)/ZIF-8 exhibits similar instability as C-(Fe$(NO_3)_3$+FePc$(CN)_8$)/ZIF-8 (Figure S26). The long-term stability measurements for 10 h indicate that C-FePc$(CN)_8$/ZIF-8 possesses stable selectivity and activity at low current density (Figure S27a). However, significant CO selectivity drop and potential increase are observed at −5 mA cm^{-2} (Figure S27b), indicating that the stability of C-FePc$(CN)_8$/ZIF at high current density is still not optimized. Further, the atomically dispersed iron catalysts reported before also suffered from significant activity decay for CO_2RR.[48,51]

Theoretical calculations were employed to understand the stability difference. Two active site models are constructed. The first one is the bare Fe−N$_4$ site in the carbon matrix (Fe−N$_4$(B), Figure 5a), which resembles the surface active site. The
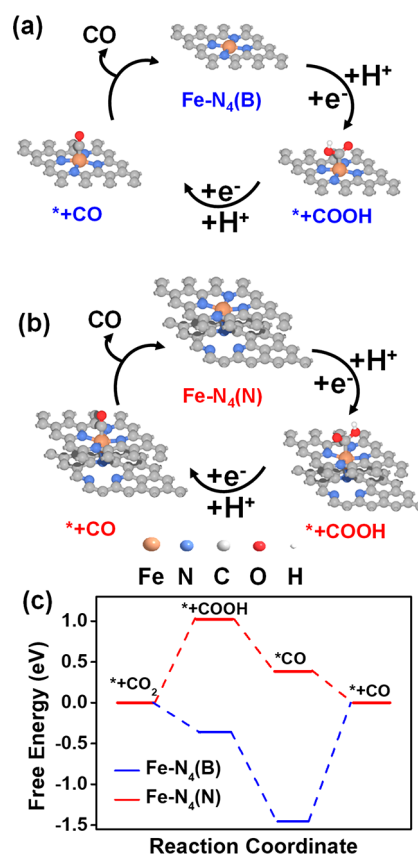

Figure 5. Proposed reaction pathways for CO_2RR on (a) Fe−N$_4$(B) sites and (b) Fe−N$_4$(N) sites. (c) Calculated free energy evolution on Fe−N$_4$(B) and Fe−N$_4$(N).

second one is the Fe−N$_4$ site with the nitrogen-doped carbon support (Fe−N$_4$(N), Figure 5b), which resembles the Fe−N$_x$ sites buried in nitrogen-doped carbon matrixes. Strong CO binding to the active site is observed on Fe−N$_4$(B) (Figure 5c), consistent with previous theoretical calculations,[33,47,52] which could account for the fast activity decay in C-(Fe$(NO_3)_3$+FePc$(CN)_8$)/ZIF-8. In contrast, CO facilely desorbs in Fe−N$_4$(N) (Figure 5c), suggesting nitrogen-doped carbon matrix benefits the stabilization of the buried active sites.

■ CONCLUSIONS

In summary, we successfully construct nitrogen-doped carbon catalysts with prevalent single iron atoms from FePc molecules-incorporated ZIF-8 for ORR and CO_2RR. The high stability of the FePc molecule and encapsulation of the ZIF framework can efficiently prevent aggregation of iron species during the high-temperature carbonization process. Cyano substitution on FePc molecules can further improve the catalytic activities due to the enhanced encapsulation of the molecules and formation of the active sites. It is also found that the ORR activities of the prepared catalysts in acidic condition are more related to the surface Fe−N$_x$ content rather than the bulk iron content. Adding Fe$(NO_3)_3$ can efficiently enhance

the surface $Fe-N_x$ content, and the afforded C-(Fe-$(NO_3)_3$+$FePc(CN)_8$)/ZIF-8 exhibits high activities in both alkaline ($E_{1/2}$ = 0.910 V) and acidic media ($E_{1/2}$ = 0.811 V). Such performance is among the best for nonprecious metal-based catalysts in both alkaline and acidic conditions reported so far. Moreover, the C-$FePc(CN)_8$/ZIF-8 catalyst exhibits high activity and selectivity for CO_2RR. We also reveal that the $Fe-N_x$ sites buried in the nitrogen-doped carbon matrixes can improve the catalytic stability for CO_2RR. Our study suggests that metal phthalocyanines or other analogues in the metal organic frameworks are efficient precursors to construct single metal atom catalysts.

■ EXPERIMENTAL SECTION

Chemicals and Materials. $Zn(NO_3)_2\cdot6H_2O$ (99.9%, Aladdin), $Fe(NO_3)_3\cdot9H_2O$ (98.0%, Aladdin), 2-methylimidazole (2-MeIm, 98.0%, Adamas), iron(III) acetylacetonate ($Fe(AcAc)_3$, 98.0%, Aladdin), iron(II) phthalocyanine (FePc, 97.0%, Aladdin), N,N-dimethylformamide (DMF, 99.5%, Aladdin), methanol (MeOH, AR, Xilong), tetracyanobenzene (TCB, 98.0%, J&K), 1,8-diazabicyclo[5.4.0]undec-7-ene (DBU, 98.0% J&K), iron(II) acetate ($Fe(OAc)_2$, 98.0%, J&K), sulfolane (99.0% Aladdin), potassium hydroxide (KOH, 90.0%, Aladdin), perchloric acid ($HClO_4$, 70.0%, Aladdin), and 20% Pt/C (Alfa Aesar) were used without further purification. Milli-Q water of 18 MΩ·cm was used in all experiments.

Synthesis of $FePc(CN)_8$. $FePc(CN)_8$ was synthesized by a reported method with some modifications.[50] TCB (14.2 mmol) and $Fe(OAc)_2$ (4.23 mmol) were reacted with a few drops of DBU in 50 mL of sulfolane at 135 °C for 2 h. The reaction mixture was precipitated from methanol, and the resulting dark green solid was collected and washed with ether. The purified product was obtained by Soxhlet extraction with methanol followed by filitration with DMF and drying after rotary evaporation. ESI-mass (m/z): 768.04834 (M^-). Analysis: $C_{40}H_8N_{16}Fe$, 768.04673. UV−vis: λ_{max} (DMF) 693 nm (the absorption spectrum is shown in Figure S28).

Synthesis of C-ZIF-8. 2-MeIm (24 mmol) in 30 mL of MeOH was added into the $Zn(NO_3)_2$ solution (6 mmol of $Zn(NO_3)_2\cdot6H_2O$ in 120 mL of MeOH). The mixed solution was stirred for 18 h at RT. The precipitate was collected by centrifuging and alternatively washed with DMF and then MeOH three times. Finally, the precipitate was lyophilized. Then the dried power was heated to 1000 °C with a ramping rate of 5 °C min^{-1}, maintained at that temperature for 3 h under an Ar flow of 100 sccm, and then cooled to RT. The black power was directly used without any other treatments.

Synthesis of C-FePc/ZIF-8. 2-MeIm (24 mmol) in 30 mL of MeOH was added into the $Zn(NO_3)_2$ solution (6 mmol $Zn(NO_3)_2\cdot6H_2O$ in 120 mL of MeOH). Then a solution of FePc (0.10 mmol) dissolved in 10 mL of DMF was added to the above solution. The mixed solution was stirred for 18 h. The precipitate was collected by centrifuging and alternatively washed with DMF and then MeOH three times. Finally, the precipitate was lyophilized. Then the dried power was heated to 1000 °C with a ramping rate of 5 °C min^{-1}, maintained at that temperature for 3 h under an Ar flow of 100 sccm, and then cooled to RT. The black power was directly used without any other treatments.

Synthesis of C-$FePc(CN)_8$/ZIF-8. It was synthesized by a similar method as C-FePc/ZIF-8 by replacing FePc to $FePc(CN)_8$.

Synthesis of C-(Fe$(NO_3)_3$+$FePc(CN)_8$)/ZIF-8. It was synthesized by a similar method as C-FePc/ZIF-8 by replacing $Zn(NO_3)_2\cdot6H_2O$ with ($Zn(NO_3)_2\cdot6H_2O$ (5.88 mmol) + 0.12 mmol $Fe(NO_3)_3\cdot9H_2O$) and also replacing FePc with $FePc(CN)_8$.

Synthesis of C-$FePc(CN)_8$@ZIF-8. The synthesized ZIF-8 (384 mg) was dispersed in 150 mL of MeOH. $FePc(CN)_8$ (0.10 mmol) dissolved in 10 mL of DMF was added to the MeOH solution, and the mixed solution was stirred for 18 h. The precipitate was collected by centrifuging and alternatively washed with DMF and then MeOH three times. Finally, the precipitate was lyophilized. Then the dried powder was heated to 1000 °C with a ramping rate of 5 °C min^{-1}, maintained at that temperature for 3 h under an Ar flow of 100 sccm, and then cooled to RT. The black power was directly used without any other treatments.

Synthesis of C-$Fe(AcAc)_3$/ZIF-8. It was synthesized by a similar method as C-FePc/ZIF-8 by replacing FePc with $Fe(AcAc)3$ (0.10 mmol).

A CHI760E electrochemical workstation (Shanghai, China) was used for electrochemical characterization. For ORR measurements, 4 mg of catalyst and 10 μL of 5 wt % Nafion solution (12% of Nafion to catalyst ratio) were dispersed in ethanol (1 mL for the prepared catalysts, 4 mg/mL; 4 mL for Pt/C, 1 mg/mL) assisted by ultrasonication for ~60 min to form a homogeneous ink. Then the catalyst ink (10 μL for the prepared catalysts in alkaline condition, 30 μL for the prepared catalysts in acidic condition, 20 μL for Pt/C) was loaded onto a glassy carbon (GC) electrode that was 5 mm in diameter. The LSV measurements (5 mV s^{-1}) were conducted with a three-electrode system. The working electrode was the glassy carbon electrode loaded with the catalyst, the refereence electrode was the saturated calomel electrode (SCE), and the counter electrode is a graphite rod. The SCE was calibrated with a reversible hydrogen electrode (RHE). Before the start of an experiment, oxygen gas was bubbled in the electrolyte for more than 30 min to achieve the saturated state. During the electochemical measurements, an oxygen flow was maintained in the system to keep the oxygen-saturated condition. In control experiments, an Ar flow was applied to the electro-chemical cell.

The J_K was determined by the Koutecky−Levich equation

$$\frac{1}{J} = \frac{1}{J_K} + \frac{1}{J_L}$$

where J is the measured current density, J_K is the kinetic current density, and J_L is the limiting current density.

For the RRDE measurements, the disk electrode was scanned from 1.10 to 0.20 V at 5 mV s^{-1}, and the ring potential was kept at 1.5 V. The following equation is employed to calculate peroxide yield (% HO_2^-) and the electron transfer number (n)

$$\%HO_2^- = 200 \times \frac{I_r/N}{I_d + I_r/N}$$

$$n = 4 \times \frac{I_d}{I_d + I_r/N}$$

where I_r is ring current, I_d is disk current, and N is current collection efficiency of the Pt ring.

The RDE and RRDE data for the prepared catalysts were recorded in cathodic scans, while those of the Pt catalyst were recorded in anodic scans.

For the CO_2RR measurements, 4 mg of catalyst and 10 μL of 5 wt % Nafion solution (12% of Nafion to catalyst ratio) were dispersed in ethanol (1 mL for the prepared catalysts, 4 mg/mL) assisted by ultrasonication for ~60 min. Then 50 μL of catalyst ink was loaded onto carbon fiber paper (0.4 mg cm^{-2}). The CV and chronopotentiometry tests were conducted with a three-electrode system. The working electrode is the catalyst-coated carbon fiber paper electrode, the reference electrode is the saturated Ag/AgCl electrode, and the counter electrode is a graphite rod (Figure S29). The electrolyte was 0.5 M $KHCO_3$ solution saturated with CO_2 (pH 7.2). The Nernst equation is employed to convert the measured potentials to RHE scale. Electrolytes were saturated with high-purity CO_2 gas (99.999%) for 30 min prior to the start of each experiment. A CO_2 gas flow (99.999%) with a flow rate of 8 sccm was delivered into the cathodic compartment of the measured system. The gas products were analyzed by gas chromatography (GC, SRI Instruments) (Figure S29).

ASSOCIATED CONTENT

Ⓢ Supporting Information

The Supporting Information is available free of charge on the ACS Publications website at DOI: 10.1021/acscatal.9b01617.

Instrumentation, computational methods; FT-IR spectra; XRD patterns; TEM images; N_2 adsorption/desorption plots and pore distribution of the carbonized products; HAADF-STEM images; STEM images; XANES and EXAFS spectra; TGA; stability tests; ORR polarization plots; XPS survey spectra; N 1s spectra; C 1s spectra; Tafel slopes; chronoamperometry; long-term operation stabilities; UV−vis spectra; photographs of the measurement setup for the CO_2 reduction reaction; BET surface area, mean pore diameter, and pore volume for different catalysts; metal content of the precursors and prepared catalysts determined from the ICP-MS test; measured nitrogen contents of the prepared catalysts by EA and XPS; comparison of the ORR catalytic performance in acidic conditions; comparison of the ORR catalytic performance in alkaline conditions; comparison of the CO_2 catalytic performance between C-FePc(CN)$_8$/ZIF-8 and reported Fe−N−C catalysts in aqueous media; references (PDF)

AUTHOR INFORMATION

Corresponding Authors
*E-mail: gum@sustech.edu.cn.
*E-mail: zhenxing.feng@oregonstate.edu.
*E-mail: liangyy@sustech.edu.cn.

ORCID Ⓞ
Meng Gu: 0000-0002-5126-9611
Zhenxing Feng: 0000-0001-7598-5076
Yongye Liang: 0000-0002-7416-8792

Author Contributions
The manuscript was prepared with the contributions from all authors. All authors have given approval to the final version of the manuscript.

Notes

REFERENCES
(1) Seh, Z. W.; Kibsgaard, J.; Dickens, C. F.; Chorkendorff, I.; Norskov, J. K.; Jaramillo, T. F. Combining Theory and Experiment in Electrocatalysis: Insights into Materials Design. *Science* **2017**, *355*, eaad4998.

(2) Shao, M.; Chang, Q.; Dodelet, J. P.; Chenitz, R. Recent Advances in Electrocatalysts for Oxygen Reduction Reaction. *Chem. Rev.* **2016**, *116*, 3594−3657.

(3) Liang, Y.; Li, Y.; Wang, H.; Dai, H. Strongly Coupled Inorganic/Nanocarbon Hybrid Materials for Advanced Electrocatalysis. *J. Am. Chem. Soc.* **2013**, *135*, 2013−2036.

(4) Stephens, I. E. L.; Bondarenko, A. S.; Grønbjerg, U.; Rossmeisl, J.; Chorkendorff, I. Understanding the Electrocatalysis of Oxygen Reduction on Platinum and Its Alloys. *Energy Environ. Sci.* **2012**, *5*, 6744−6762.

(5) Wang, C.; Chi, M.; Li, D.; Strmcnik, D.; van der Vliet, D.; Wang, G.; Komanicky, V.; Chang, K. C.; Paulikas, A. P.; Tripkovic, D.; Pearson, J.; More, K. L.; Markovic, N. M.; Stamenkovic, V. R. Design and Synthesis of Bimetallic Electrocatalyst with Multilayered Pt-Skin Surfaces. *J. Am. Chem. Soc.* **2011**, *133*, 14396−14403.

(6) Zhao, X.; Chen, S.; Fang, Z.; Ding, J.; Sang, W.; Wang, Y.; Zhao, J.; Peng, Z.; Zeng, J. Octahedral Pd@Pt1.8Ni Core-Shell Nanocrystals with Ultrathin PtNi Alloy Shells as Active Catalysts for Oxygen Reduction Reaction. *J. Am. Chem. Soc.* **2015**, *137*, 2804−2807.

(7) Zhang, J.; Zhao, Z.; Xia, Z.; Dai, L. A Metal-free Bifunctional Electrocatalyst for Oxygen Reduction and Oxygen Evolution Reactions. *Nat. Nanotechnol.* **2015**, *10*, 444−452.

(8) Guo, J.; Li, Y.; Cheng, Y.; Dai, L.; Xiang, Z. Highly Efficient Oxygen Reduction Reaction Electrocatalysts Synthesized under Nanospace Confinement of Metal-Organic Framework. *ACS Nano* **2017**, *11*, 8379−8386.

(9) Liu, Z.; Sun, F.; Gu, L.; Chen, G.; Shang, T.; Liu, J.; Le, Z.; Li, X.; Wu, H. B.; Lu, Y. Post Iron Decoration of Mesoporous Nitrogen-Doped Carbon Spheres for Efficient Electrochemical Oxygen Reduction. *Adv. Energy Mater.* **2017**, *7*, 1701154.

(10) Liang, Y.; Wang, H.; Zhou, J.; Li, Y.; Wang, J.; Regier, T.; Dai, H. Covalent Hybrid of Spinel Manganese-Cobalt Oxide and Graphene as Advanced Oxygen Reduction Electrocatalysts. *J. Am. Chem. Soc.* **2012**, *134*, 3517−3523.

(11) Chung, H. T.; Cullen, D. A.; Higgins, D.; Sneed, B. T.; Holby, E. F.; More, K. L.; Zelenay, P. Direct Atomic-Level Insight into the Active Sites of a High-Performance PGM-Free ORR Catalyst. *Science* **2017**, *357*, 479−484.

(12) Li, J.; Ghoshal, S.; Liang, W.; Sougrati, M.-T.; Jaouen, F.; Halevi, B.; McKinney, S.; McCool, G.; Ma, C.; Yuan, X.; Ma, Z.-F.;

Mukerjee, S.; Jia, Q. Structural and Mechanistic Basis for the High Activity of Fe−N−C Catalysts Toward Oxygen Reduction. *Energy Environ. Sci.* **2016**, *9*, 2418−2432.

(13) Lefevre, M.; Proietti, E.; Jaouen, F.; Dodelet, J. P. Iron-Based Catalysts with Improved Oxygen Reduction Activity in Polymer ElectrolyteFuel Cells. *Science* **2009**, *324*, 71−74.

(14) Proietti, E.; Jaouen, F.; Lefevre, M.; Larouche, N.; Tian, J.; Herranz, J.; Dodelet, J. P. Iron-Based Cathode Catalyst with Enhanced Power Density in Polymer Electrolyte Membrane Fuel Cells. *Nat. Commun.* **2011**, *2*, 416.

(15) Lai, Q.; Zheng, L.; Liang, Y.; He, J.; Zhao, J.; Chen, J. Metal−Organic-Framework-Derived Fe−N/C Electrocatalyst with Five-Coordinated Fe−Nx Sites for Advanced Oxygen Reduction in Acid Media. *ACS Catal.* **2017**, *7*, 1655−1663.

(16) Wan, G.; Yang, C.; Zhao, W.; Li, Q.; Wang, N.; Li, T.; Zhou, H.; Chen, H.; Shi, J. Anion-Regulated Selective Generation of Cobalt Sites in Carbon: Toward Superior Bifunctional Electrocatalysis. *Adv. Mater.* **2017**, *29*, 1703436.

(17) Xiao, M.; Zhu, J.; Feng, L.; Liu, C.; Xing, W. Meso/Macroporous Nitrogen-Doped Carbon Architectures with Iron Carbide Encapsulated in Graphitic Layers as an Efficient and Robust Catalyst for the Oxygen Reduction Reaction in Both Acidic and Alkaline Solutions. *Adv. Mater.* **2015**, *27*, 2521−2527.

(18) Hu, Y.; Jensen, J. O.; Zhang, W.; Cleemann, L. N.; Xing, W.; Bjerrum, N. J.; Li, Q. Hollow Spheres of Iron Carbide Nanoparticles Encased in Graphitic Layers as Oxygen Reduction Catalysts. *Angew. Chem., Int. Ed.* **2014**, *53*, 3675−3679.

(19) Yang, G.; Choi, W.; Pu, X.; Yu, C. Scalable Synthesis of Bi-Functional High-Performance Carbon Nanotube Sponge Catalysts and Electrodes with Optimum C−N−Fe Coordination for Oxygen Reduction Reaction. *Energy Environ. Sci.* **2015**, *8*, 1799−1807.

(20) Chen, Y.; Ji, S.; Wang, Y.; Dong, J.; Chen, W.; Li, Z.; Shen, R.; Zheng, L.; Zhuang, Z.; Wang, D.; Li, Y. Isolated Single Iron Atoms Anchored on N-Doped Porous Carbon as an Efficient Electrocatalyst for the Oxygen Reduction Reaction. *Angew. Chem., Int. Ed.* **2017**, *56*, 6937−6941.

(21) Zhang, H.; Hwang, S.; Wang, M.; Feng, Z.; Karakalos, S.; Luo, L.; Qiao, Z.; Xie, X.; Wang, C.; Su, D.; Shao, Y.; Wu, G. Single Atomic Iron Catalysts for Oxygen Reduction in Acidic Media: Particle Size Control and Thermal Activation. *J. Am. Chem. Soc.* **2017**, *139*, 14143−14149.

(22) Jasinski, P. A New Fuel Cell Cathode Catalyst. *Nature* **1964**, *201*, 1212−1213.

(23) Zhang, Z.; Sun, J.; Wang, F.; Dai, L. Efficient Oxygen Reduction Reaction (ORR) Catalysts Based on Single Iron Atoms Dispersed on a Hierarchically Structured Porous Carbon Framework. *Angew. Chem., Int. Ed.* **2018**, *57*, 9038−9043.

(24) Zhang, X.; Wu, Z.; Zhang, X.; Li, L.; Li, Y.; Xu, H.; Li, X.; Yu, X.; Zhang, Z.; Liang, Y.; Wang, H. Highly Selective and Active CO2 Reduction Electrocatalysts Based on Cobalt Phthalocyanine/Carbon Nanotube Hybrid Structures. *Nat. Commun.* **2017**, *8*, 14675.

(25) Cao, R.; Thapa, R.; Kim, H.; Xu, X.; Gyu Kim, M.; Li, Q.; Park, N.; Liu, M.; Cho, J. Promotion of Oxygen Reduction by a Bio-Inspired Tethered Iron Phthalocyanine Carbon Nanotube-Based Catalyst. *Nat. Commun.* **2013**, *4*, 2076.

(26) Hijazi, I.; Bourgeteau, T.; Cornut, R.; Morozan, A.; Filoramo, A.; Leroy, J.; Derycke, V.; Jousselme, B.; Campidelli, S. Carbon Nanotube-Templated Synthesis of Covalent Porphyrin Network for Oxygen Reduction Reaction. *J. Am. Chem. Soc.* **2014**, *136*, 6348−6354.

(27) Wu, Z. S.; Chen, L.; Liu, J.; Parvez, K.; Liang, H.; Shu, J.; Sachdev, H.; Graf, R.; Feng, X.; Mullen, K. High-Performance Electrocatalysts for Oxygen Reduction Derived from Cobalt Porphyrin-Based Conjugated Mesoporous Polymers. *Adv. Mater.* **2014**, *26*, 1450−1455.

(28) Yin, H.; Zhang, C.; Liu, F.; Hou, Y. Hybrid of Iron Nitride and Nitrogen-Doped Graphene Aerogel as Synergistic Catalyst for Oxygen Reduction Reaction. *Adv. Funct. Mater.* **2014**, *24*, 2930−2937.

(29) Sa, Y. J.; Seo, D. J.; Woo, J.; Lim, J. T.; Cheon, J. Y.; Yang, S. Y.; Lee, J. M.; Kang, D.; Shin, T. J.; Shin, H. S.; Jeong, H. Y.; Kim, C. S.; Kim, M. G.; Kim, T. Y.; Joo, S. H. A General Approach to Preferential Formation of Active Fe-Nx Sites in Fe-N/C Electrocatalysts for Efficient Oxygen Reduction Reaction. *J. Am. Chem. Soc.* **2016**, *138*, 15056.

(30) Choi, C. H.; Lim, H. K.; Chung, M. W.; Chon, G.; Sahraie, N. R.; Altin, A.; Sougrati, M. T.; Stievano, L.; Oh, H. S.; Park, E. S.; Luo, F.; Strasser, P.; Drazic, G.; Mayrhofer, K. J. J.; Kim, H.; Jaouen, F. The Achilles' Heel of Iron-based Catalysts During Oxygen Reduction in an Acidic Medium. *Energy Environ. Sci.* **2018**, *11*, 3176−3182.

(31) Weng, Z.; Wu, Y.; Wang, M.; Jiang, J.; Yang, K.; Huo, S.; Wang, X. F.; Ma, Q.; Brudvig, G. W.; Batista, V. S.; Liang, Y.; Feng, Z.; Wang, H. Active Sites of Copper-Complex Catalytic Materials for Electrochemical Carbon Dioxide Reduction. *Nat. Commun.* **2018**, *9*, 415.

(32) Zitolo, A.; Goellner, V.; Armel, V.; Sougrati, M. T.; Mineva, T.; Stievano, L.; Fonda, E.; Jaouen, F. Identification of Catalytic Sites for Oxygen Reduction in Iron- and Nitrogen-Doped Graphene Materials. *Nat. Mater.* **2015**, *14*, 937−942.

(33) Ju, W.; Bagger, A.; Hao, G. P.; Varela, A. S.; Sinev, I.; Bon, V.; Roldan Cuenya, B.; Kaskel, S.; Rossmeisl, J.; Strasser, P. Understanding Activity and Selectivity of Metal-Nitrogen-Doped Carbon Catalysts for Electrochemical Reduction of CO2. *Nat. Commun.* **2017**, *8*, 944.

(34) Jiang, P.; Chen, J.; Wang, C.; Yang, K.; Gong, S.; Liu, S.; Lin, Z.; Li, M.; Xia, G.; Yang, Y.; Su, J.; Chen, Q. Tuning the Activity of Carbon for Electrocatalytic Hydrogen Evolution via an Iridium-Cobalt Alloy Core Encapsulated in Nitrogen-Doped Carbon Cages. *Adv. Mater.* **2018**, *30*, 1705324.

(35) Lepper, M.; Kobl, J.; Zhang, L.; Meusel, M.; Holzel, H.; Lungerich, D.; Jux, N.; de Siervo, A.; Meyer, B.; Steinruck, H. P.; Marbach, H. Controlling the Self-Metalation Rate of Tetraphenylporphyrins on Cu(111) via Cyano Functionalization. *Angew. Chem., Int. Ed.* **2018**, *57*, 10074−10079.

(36) Kuhn, P.; Forget, A.; Su, D. S.; Thomas, A.; Antonietti, M. From Microporous Regular Frameworks to Mesoporous Materials with Ultrahigh Surface Area Dynamic Reorganization of Porous Polymer Networks. *J. Am. Chem. Soc.* **2008**, *130*, 13333−13337.

(37) Jiang, H. L.; Jiao, L.; Wan, G.; Zhang, R.; Zhou, H.; Yu, S. H. From MOFs to Single Fe Atoms Implanted N-Doped Porous Carbons: Efficient Oxygen Reduction in Both Alkaline and Acidic Media. *Angew. Chem., Int. Ed.* **2018**, *57*, 8525−8529.

(38) Yasuda, S.; Furuya, A.; Uchibori, Y.; Kim, J.; Murakoshi, K. Iron-Nitrogen-Doped Vertically Aligned Carbon Nanotube Electrocatalyst for the Oxygen Reduction Reaction. *Adv. Funct. Mater.* **2016**, *26*, 738−744.

(39) Yang, Y.; Mao, K.; Gao, S.; Huang, H.; Xia, G.; Lin, Z.; Jiang, P.; Wang, C.; Wang, H.; Chen, Q. O-,N-Atoms-Coordinated Mn Cofactors within a Graphene Framework as Bioinspired Oxygen Reduction Reaction Electrocatalysts. *Adv. Mater.* **2018**, *30*, 1801732.

(40) Wang, X.; Zhang, H.; Lin, H.; Gupta, S.; Wang, C.; Tao, Z.; Fu, H.; Wang, T.; Zheng, J.; Wu, G.; Li, X. Directly Converting Fe-Doped Metal−Organic Frameworks into Highly Active and Stable Fe-N-C Catalysts for Oxygen Reduction in Acid. *Nano Energy* **2016**, *25*, 110−119.

(41) Liang, H. W.; Wei, W.; Wu, Z. S.; Feng, X.; Mullen, K. Mesoporous Metal-Nitrogen-Doped Carbon Electrocatalysts for Highly Efficient Oxygen Reduction Reaction. *J. Am. Chem. Soc.* **2013**, *135*, 16002−16005.

(42) Wang, X. X.; Cullen, D. A.; Pan, Y. T.; Hwang, S.; Wang, M.; Feng, Z.; Wang, J.; Engelhard, M. H.; Zhang, H.; He, Y.; Shao, Y.; Su, D.; More, K. L.; Spendelow, J. S.; Wu, G. Nitrogen-Coordinated Single Cobalt Atom Catalysts for Oxygen Reduction in Proton Exchange Membrane Fuel Cells. *Adv. Mater.* **2018**, *30*, 1706758.

(43) Hu, B.-C.; Wu, Z.-Y.; Chu, S.-Q.; Zhu, H.-W.; Liang, H.-W.; Zhang, J.; Yu, S.-H. SiO2-Protected Shell Mediated Templating Synthesis of Fe−N-doped Carbon Nanofibers and Their Enhanced

Oxygen Reduction Reaction Performance. *Energy Environ. Sci.* **2018**, *11*, 2208−2215.

(44) Stamenkovic, V.; Schmidt, T. J.; Ross, P. N.; Markovic, N. M. Surface Composition Effects in Electrocatalysis: Kinetics of Oxygen Reduction on Well-Defined Pt_3Ni and Pt_3Co Alloy Surfaces. *J. Phys. Chem. B* **2002**, *106*, 11970−11979.

(45) Holewinski, A.; Linic, S. Elementary Mechanisms in Electrocatalysis: Revisiting the ORR Tafel Slope. *J. Electrochem. Soc.* **2012**, *159*, H864−H870.

(46) Zagal, J. H.; Koper, M. T. M. Reactivity Descriptors for the Activity of Molecular MN4 Catalysts for the Oxygen Reduction Reaction. *Angew. Chem., Int. Ed.* **2016**, *55*, 14510−14521.

(47) Pan, F.; Zhang, H.; Liu, K.; Cullen, D.; More, K.; Wang, M.; Feng, Z.; Wang, G.; Wu, G.; Li, Y. Unveiling Active Sites of CO_2 Reduction on Nitrogen-Coordinated and Atomically Dispersed Iron and Cobalt Catalysts. *ACS Catal.* **2018**, *8*, 3116−3122.

(48) Zhang, C. H.; Yang, S. Z.; Wu, J. J.; Liu, M. J.; Yazdi, S.; Ren, M. Q.; Sha, J. W.; Zhong, J.; Nie, K. Q.; Jalilov, A. S.; Li, Z. Y.; Li, H. M.; Yakobson, B. I.; Wu, Q.; Ringe, E. L.; Xu, H.; Ajayan, P. M.; Tour, J. M. Electrochemical CO_2 Reduction with Atomic Iron-Dispersed on Nitrogen-Doped Graphene. *Adv. Energy Mater.* **2018**, *8*, 1703487.

(49) Maurin, A.; Robert, M. Noncovalent Immobilization of a Molecular Iron-Based Electrocatalyst on Carbon Electrodes for Selective, Efficient CO_2-to-CO Conversion in Water. *J. Am. Chem. Soc.* **2016**, *138*, 2492−2495.

(50) Ye, Y.; Cai, F.; Li, H.; Wu, H.; Wang, G.; Li, Y.; Miao, S.; Xie, S.; Si, R.; Wang, J.; Bao, X. Surface Functionalization of ZIF-8 with Ammonium Ferric Citrate toward High Exposure of Fe-N Active Sites for Efficient Oxygen and Carbon Dioxide Electroreduction. *Nano Energy* **2017**, *38*, 281−289.

(51) Choi, J.; Wagner, P.; Jalili, R.; Kim, J.; MacFarlane, D. R.; Wallace, G. G.; Officer, D. L. A Porphyrin/Graphene Framework: A Highly Efficient and Robust Electrocatalyst for Carbon Dioxide Reduction. *Adv. Energy Mater.* **2018**, *8*, 1801280.

(52) Varela, A. S.; RanjbarSahraie, N.; Steinberg, J.; Ju, W.; Oh, H. S.; Strasser, P. Metal-Doped Nitrogenated Carbon as an Efficient Catalyst for Direct CO_2 Electroreduction to CO and Hydrocarbons. *Angew. Chem., Int. Ed.* **2015**, *54*, 10758−10762.